water

MDPI

Article

Pre-Treatment and Turbidity Reduction of Sea Waters Using New Composite Ceramic Microfiltration Membranes with Iron Oxide Additive

Mehran Yousefi [1], Mohsen Abbasi [1,*], Mohammad Akrami [2,*] and Mika Sillanpää [3,4,5]

[1] Sustainable Membrane Technology Research Group, Department of Chemical Engineering, Faculty of Petroleum, Gas and Petrochemical Engineering, Persian Gulf University, Bushehr 75169, Iran
[2] Department of Engineering, University of Exeter, Exeter EX4 4QF, UK
[3] International Research Centre of Nanotechnology for Himalayan Sustainability (IRCNHS), Shoolini University, Solan 173212, Himachal Pradesh, India
[4] Zhejiang, Rongsheng Environmental Protection Paper, Joint Stock Co., Ltd., No.588 Zhennan East RoadPinghu, Economic Development Zone, Pinghu 314213, China
[5] Department of Civil Engineering, University Centre for Research & Development, Chandigarh University, Gharuan, Mohali 140413, Punjab, India
* Correspondence: m.abbasi@pgu.ac.ir (M.A.); m.akrami@exeter.ac.uk (M.A.)

Abstract: In this research, an experimental study was carried out on the pre-treatment and turbidity removal of Persian Gulf water using cross flow microfiltration by new composite ceramic membranes. Three types of tubular microfiltration composite ceramic membranes that consisted of Mullite, Mullite/SiC, and Mullite/SiC/Fe_2O_3 with different compositions were fabricated at relatively low temperature (1250 °C) with extrusion and sintering for this purpose. Furthermore, changes in porosity, pore size, and mechanical strength were compared in Mullite membranes and composite membranes to find the most suitable membrane for turbidity removal from seawater. According to the results, the most suitable synthetic membrane was M/SiC/Fe10 membrane with 60:30:10 ratios of mullite, silicon carbide, and iron oxide with 64.6 ± 2% porosity, average pore size of 0.54 µm, 95.4% turbidity removal, pure water permeability of 3811 L/m^2.h, and higher mechanical strength (22.4 MPa) compared to other fabricated membranes. Results of Hermia's models for fouling modeling indicated that the dominant mechanism of blocking in all membranes was standard pore blocking with the best compliance with experimental data. Therefore, results demonstrated that the addition of Fe_2O_3 to silicon carbide ceramic microfiltration membranes, with a specific weight percentage, improves their mechanical properties and membrane performance for pre-treatment of seawaters.

Keywords: ceramic membrane; silicon carbide; iron oxide; seawater pre-treatment; turbidity

Citation: Yousefi, M.; Abbasi, M.; Akrami, M.; Sillanpää, M. Pre-Treatment and Turbidity Reduction of Sea Waters Using New Composite Ceramic Microfiltration Membranes with Iron Oxide Additive. *Water* **2022**, *14*, 3475. https://doi.org/10.3390/w14213475

Academic Editor: Jesus Gonzalez-Lopez

Received: 11 October 2022
Accepted: 27 October 2022
Published: 30 October 2022

1. Introduction

Due to the water shortage and drought around the world, societies have considered desalination as an important strategy to support ever-decreasing fresh water sources in the last 40 years [1,2]. Seawater desalination is a necessary strategy for supplying potable water in many parts of the world, such as the Middle East and North Africa [3,4]. Seawater is a potential water source that can be used for household and industrial purposes, after desalination [5]. Different methods are used for seawater desalination, such as thermal and membrane processes. During these years, researchers have found that seawater desalination by membrane processes such as reverse osmosis (RO) is more feasible compared to other methods [6,7]. However, the main problem of membrane desalination technology is the presence of particles and colloids, microorganisms, and organic materials that cause sedimentation on the membrane surface. Therefore, the correct selection of the pre-treatment method is one of the determining solutions for the success or failure of seawater desalination [5]. Seawater desalination is conducted for the reduction in turbidity,

microorganisms, colloidal pollutants, Total Dissolved Solids (TDS), and Silt Density Index (SDI) of raw seawater, to acceptable levels and makes it suitable for the RO process [6]. Many common processes are utilized for seawater pre-treatment before RO desalination. However, membrane-based technology, especially microfiltration (MF), has many advantages over other methods including high flux, lower costs and spaces, and no need for chemicals. Furthermore, MF has a high performance in improving sea water quality, especially for the elimination of colloids, suspended particles, microorganisms, and turbidity removal [8,9]. Results of many studies show the utilization of polymer membranes for seawater pre-treatment [10,11]; however, ceramic membranes have been noticed in recent years due to their superior characteristics (high flux, high porosity, higher chemical, and mechanical strength) [12,13]. Many studies were carried out on the pre-treatment of seawater by microfiltration ceramic filters [14–18].

Dey et al. [18] investigated the pretreatment of Arabian coastal sea water using a tubular alumina-based ceramic MF membrane with a 19-channel configuration. The results of their research indicated a decrease in turbidity to less than 1.0 NTU. Achiou et al. [14] manufactured and investigated tubular ceramic microfiltration membranes made from natural pozzolan; their membranes could remove 98.25% of seawater turbidity. Mouiya et al. [16] manufactured and studied natural clay and Moroccan phosphate-based ceramic microfiltration membranes for seawater desalination. Results of this study showed 99.6% turbidity removal. Ceramic microfiltration membranes were manufactured from natural phosphate by Belgad et al. [8] and could eliminate 98% of seawater turbidity. Xavier et al. [19] studied the manufacturing of microfiltration ceramic filters from steel slag to be used in pre-treatment and turbidity removal from seawater. Results of their research indicated 95.37% removal of turbidity by the manufactured ceramic filters.

As the results of these investigations present, ceramic membranes have a very high ability to remove seawater turbidity; however, despite the fantastic performance of microfiltration membranes in seawater desalination, fouling of membranes due to their large pores causes a reduction in their performance including flux and considerably affects their utilization [20]. Considering the importance and necessity of minimizing the sediment formation on membranes to increase flux, improvement of the treatment efficiency, decrease in the cost and energy consumption, and generally optimizing and controlling the filtration process, different mechanisms were proposed and investigated. Some theoretical, experimental, and semi-experimental models exist in the literature that are used to predict the reduction in flux. Both theoretical and empirical models cannot favorably predict the time dependence of flux reduction without using experimental data and an explanation of the sedimentation mechanism. The most commonly used model for studying fouling in MF membranes is the Hermia's models. Hermia's models are a one-parameter, semi-experimental model in which the parameters have specific physical meanings. These models were successful at explaining the fouling mechanism and precisely predicting the reduction of flux over time [21,22].

Silicon carbide (SiC) ceramic microfiltration membranes have attracted significant attention due to their favorable properties of fantastic mechanical strength, porous structure, anti-corrosion performance, high chemical resistance, negative surface charge, and high hydrophobicity [23,24]. However, the main problem with these membranes is their high sintering temperature of 2000 °C which consumes much energy, increases the costs of large-scale production, and limits their industrial usage. This problem can be solved by using geomaterials such as clay, phosphate, natural zeolite, kaolin, and pozzolan and manufacturing low-cost composite ceramic membranes [25–30]. The addition of sintering-aid materials changes the eutectic temperature and viscosity; therefore, it affects morphology, and the microstructure of SiC ceramic filters, and reduces the sintering temperature and decreases the cost [31,32].

Kaolin is a preferred raw material for developing low-cost porous ceramic filters due to its crystalline structure, chemical composition, and mineralogical characteristics [33].

There has been no investigation until now on the elimination of turbidity from seawater using SiC composite membranes. Therefore, in this research, we study the development of low-cost SiC membranes with desirable characteristics for pre-treatment of sea water. Thus, in this study, low-cost kaolin was used in the structure of SiC ceramic membranes to decrease production costs, and iron oxide was utilized to enhance the flux and mechanical strength of these membranes to be employed for turbidity removal and seawater pre-treatment. For a better comparison, three types of ceramic microfiltration membranes made by extrusion and sintering with different compositions of Mullite, Mullite/SiC, and Mullite/SiC/Fe_2O_3 were employed for pre-treatment and turbidity removal of seawater. In addition, the fabricated MF ceramic membranes were evaluated by considering their porosity, pore size, percent turbidity removal, mechanical characteristics, and flux of pure water. The Hermia's models were used for the estimate of the fouling mechanism and the prediction of permit flux during the pre-treatment of seawater.

2. Materials and Methods

2.1. Raw Materials

In this research, kaolin clay powder (particle size < 30 μm) from Iran was used for the preparation of ceramic membranes. The chemical composition of kaolin is presented in Table 1. Commercial SiC powder with a mean particle size smaller than 39 μm and 98.9% purity was supplied by Taif Azarin Co. Ltd., Tehran, Iran. Starch (Merck KGaA) was used as a binding agent. The iron oxide used for the experiments had a mesh size of 400 and 98.6% purity.

Table 1. Chemical composition (wt.%) of kaolin.

Chemical Composition	wt.%
SiO_2	61.62
TiO_2	0.4
Al_2O_3	24–25
Fe_2O	0.45–0.65
K_2O	0.4
Na_2O	0.5
L.O.I	9.5–10

2.2. Preparation of Seawater

Seawater used in this work was obtained from shore water of the Persian Gulf in Bushehr city of Iran. The seawater specifications are presented in Table 2.

Table 2. Specifications of the seawater.

EC (mS/cm)	56.5 ± 0.1
TDS (ppm)	39100–41300
Turbidity (NTU)	11.64 ± 0.1
pH	8.9 ± 0.1
Salinity (psu)	40.4± 0.2
Temperature (°C)	30.2 ± 1

2.3. Microfiltration Ceramic Membranes Fabrication

In this research, seven MF ceramic membranes were made. Firstly, Kaolin, kaolin/SiC and kaolin/SiC/Fe_2O_3 with a different percentage composition described in Table 3, were blended using an electrical mixer with high speed for 15 min. Following that, 5 wt.% of starch as a binder and 32 wt.% of distilled water were added to the solid mixture. Extrusion was used to make the kaolin clay/distilled water/SiC powder/Fe_2O_3 mixture after mixing well for 2 h using a high-powered mechanical mixer. A tubular membrane with an inner diameter of 10 mm, an outer diameter of 14 mm and a length of 25 cm was created. At room temperature, the prepared membranes are completely dried for twenty-four hours and then and then sintered in an electrical furnace (The overall schematic of the membranes fabrication is shown in Figure 1).

Table 3. Characteristics of fabricated ceramic membranes.

	The wt.% of the Synthesized Membranes Constituent			**Type of Membrane**	**Length (cm)**	**Inner Diameter (mm)**	**Outer Diameter (mm)**	**Membrane Surface Area (m^2)**	**Filtration Type**
Membranes	Mullite	SiC	Fe_2O_3						
M	100	-	-	tubular ceramic membranes	25	10	14	0.004554	Cross flow
M/SiC30	70	30	-						
M/SiC20	80	20	-						
M/SiC10	90	10	-						
M/SiC/Fe20	50	30	20						
M/SiC/Fe10	60	30	10						
M/SiC/Fe5	65	30	5						

Table 3 presents the compositions and characteristics of the prepared membranes. It should be mentioned that 32 wt.% of water and 5 wt.% of starch were added as binding agents.

The synthesized tubular ceramic membranes were dried at room temperature for 48 h. Then, they were sintered in a furnace (1200C MINI LAB ELECTRIC, T-Long, China) according to Figure 2.

When the sintering process was ended, membranes were left in the furnace for eight hours to reach room temperature. If they are promptly removed from the furnace, there will be a risk of thermal shock and cracking of the membranes.

2.4. Experimental Setup

The experimental setup of the cross-flow microfiltration process was designed as shown in Figure 3. This setup was designed so that the operating pressure could be changed and controlled easily. A recycle stream was embedded for better adjustment of the stream, pressure, and mixing. The pressure of seawater on membrane surface was adjusted to 1 bar using a pressure regulator. It should be mentioned that the contact surface area of the microfiltration membrane with the feed stream was 0.004554 m^2. Furthermore, three membrane samples were employed in each test to ensure the repeatability of the experimental results; all the presented data are the arithmetic average of three related filtration data. Moreover, all the filtration tests were conducted at room temperature (25 $\pm$ 1 °C).

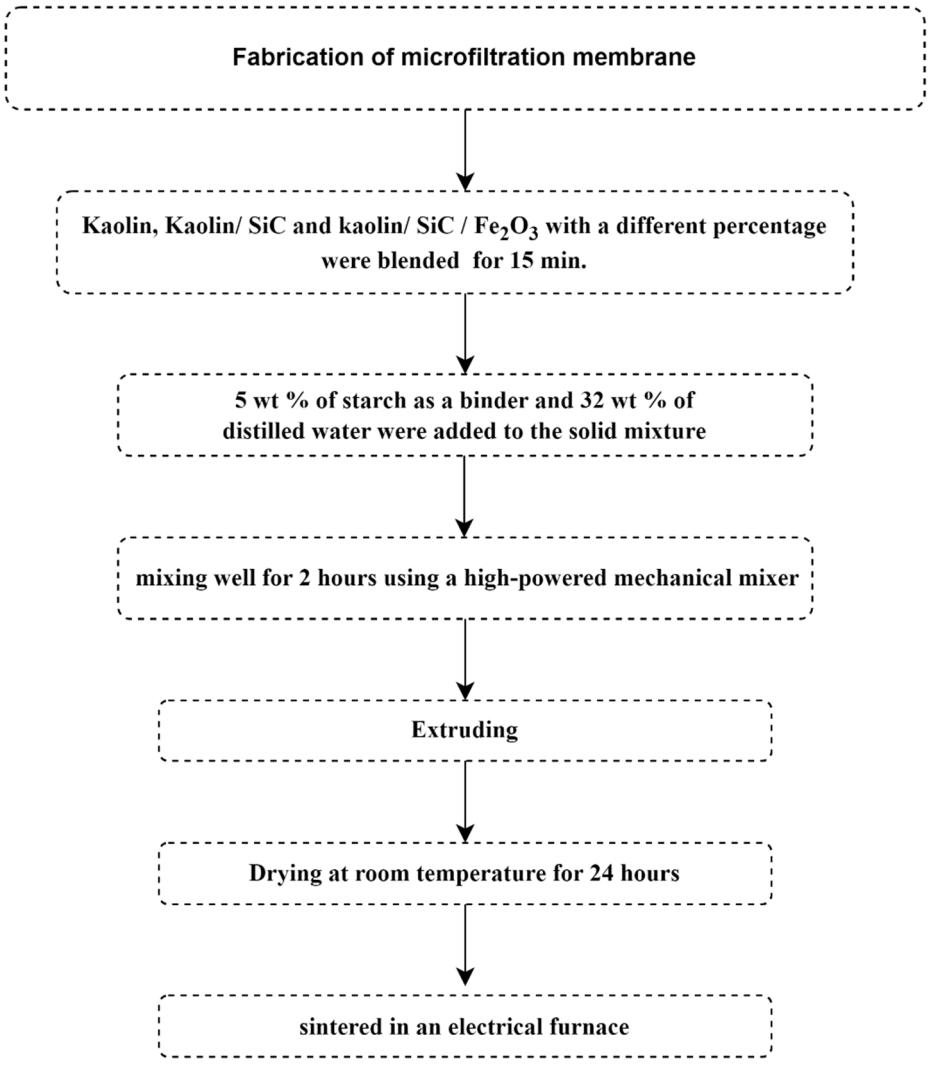

Figure 1. Schematic of preparation steps of microfiltration membranes.

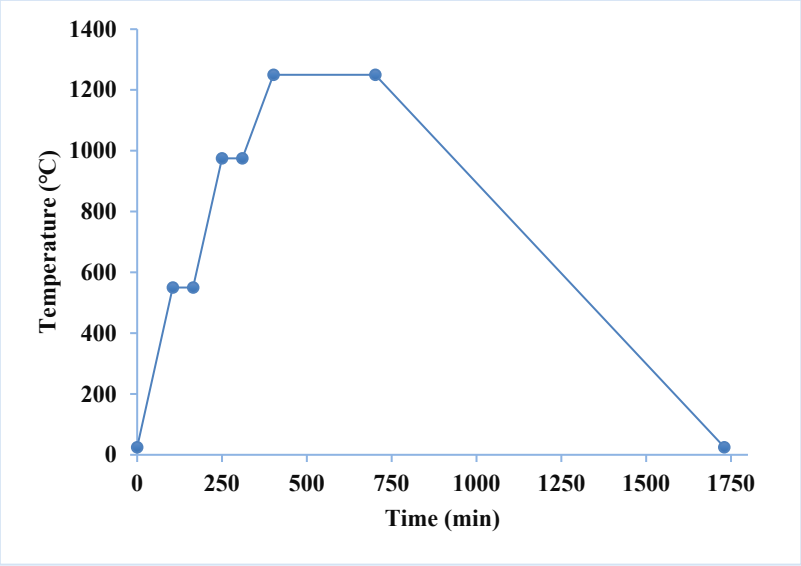

Figure 2. Sintering procedure of microfiltration membranes.

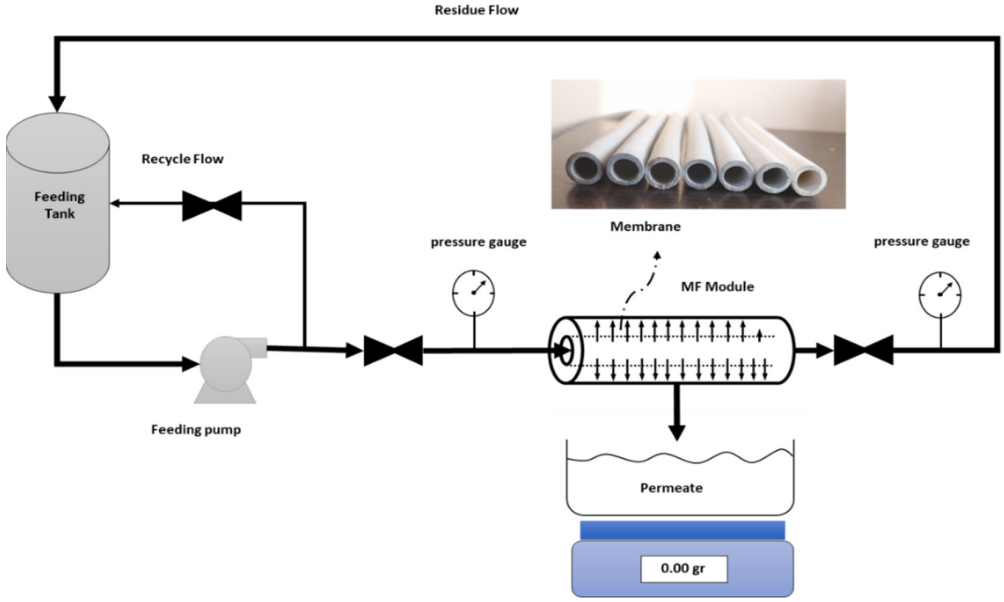

Figure 3. A schematic of the microfiltration system for seawater pre-treatment.

Different parameters are involved in a separation process that needs to be measured, such as flux of the membrane and rejection. The flux was measured at a cross flow regime. The Flux (J) was calculated from the following equation [34]:

$$\text{Flux}(J) = \frac{V}{\text{A}\,\Delta t} \tag{1}$$

where:

V:the permeate volume in (L),
A: the filtration area in (m^2),
and Δt: the time duration of filtration in (h).

3. Modeling

One of the concerns about membrane processes is the fouling of membranes, which reduces membrane efficiency, increases operating costs, and decreases the lifecycle of the membranes. Fouling mechanisms and their effect on the flux reduction during time can differ significantly depending on the type of the membrane, solution specifications, and the type of filtration (i.e., cross flow, submerged, dead-end) [21,22].

Hermia's models are among the best and most applicable models for the prediction of microfiltration flux reduction in cross-flow filtration. The formation of precipitates is modeled with the Hermia model which presents four different behaviors for membrane fouling. Complete blocking of the pores, incomplete blocking (intermediate fouling) of the pores, standard blocking of the pores, and the cake formation are the four available models [35,36].

The general equation is as follows [36]:

$$\frac{\mathrm{d}J}{\mathrm{d}t} = K(J - J_{ss})J^{2-n} \tag{2}$$

where:

J_{ss}: steady state flux of membrane,

K: constant and it depends on pressure, permeable dynamic viscosity, the blocked area, and membrane resistance.

In this equation, $n = 0$ for the filtration cake, $n = 1$ for intermediate pore blocking, $n = 1.5$ for standard blocking, and $n = 2$ for complete blocking. If the models can predict the reduction in flux of the membranes, the constant slope of the models (K) can be determined

by the linearization of the model and the selection of the greatest coefficient of determination (R^2). Therefore, the precipitation mechanism and the flux at any time and at any point of the membranes can be determined by regression of the parameters [36].

- Cake formation model

This mechanism takes place when the size of dissolved molecules is larger than the size of membrane pores and, therefore, dissolved molecules do not enter the membrane pores and form a cake layer on the membrane surface. Hence, pore blocking is neglected in this model [37]. This model is shown in Equation (3).

$$J = [(1 - Y)\ J_{ss} \frac{\sqrt{[(1 - Y)\ J_{ss}]^2 - 4(X - Y)\ {J_{ss}}^2}}{2(X - Y)} \tag{3}$$

$$X = \frac{J_0 - J_{ss}}{J_0} \tag{4}$$

$$Y = \exp\left(K\ {J_{ss}}^2 t\right) - \frac{J_{ss}}{J_0} \tag{5}$$

where J_0 is the flux at $t = 0$.

- Intermediate pore blocking model

This mechanism happens when the size of dissolved molecules is the same as membrane pore sizes; thus, the risk of membrane fouling with dissolved molecules decreases during the time [37]. This model is shown with Equation (6).

$$J = \frac{J_0\ J_{ss} B}{J_{ss} + J_0[B - 1]} \tag{6}$$

$$B = exp(K\ J_{SS} t) \tag{7}$$

- Standard pore blocking model

This mechanism takes place when dissolved molecules are smaller than membrane pores; therefore, inter-pore blocking happens. In this model, molecules cannot easily accumulate on the pore walls, but they absorb on the walls [37]. This model is presented by Equation (8).

$$\frac{1}{J^{0.5}} = \frac{1}{J_0^{0.5}} + Kt \tag{8}$$

- Complete pore blocking model

In this mechanism the molecules do not enter the pores, but instead, they block the entrance of the pores. Based on this model, any dissolved molecule that reaches the membrane surface covers the pore entrance and blocks it [37]. This model is demonstrated by Equation (9).

$$J = J_{ss} + (\ J_0 - J_{ss}\ ) \exp[(-K\ J_0\ )t] \tag{9}$$

To know the fouling mechanisms, Hermia's models were employed for cross flow filtration to investigate fouling mechanisms involved in the seawater pre-treatment process by seven fabricated microfiltration membranes. Regression results of the cross-flow filtration models were presented and compared with the experimental data.

To delineate the compliance of data with the considered model, the correlation coefficient (R^2) of each model curve was compared with the others.

4. Characterization of Fabricated Membranes

FE-SEM (TESCAN-Vega 3, made by TESCAN Co, Czech Republic) was employed to study membranes' surfaces. The 2D and 3D photos were captured by AFM (BRISK AFM, made by ARA Research, IRI) to explain the roughness of membranes' surfaces. The

phase changes, after sintering in membranes, was investigated by X-ray diffraction analysis (XRD, D8 Advance, made by BRUKER, Bremen, Germany) with a scan speed of 0.05°/s at 20–80° with 2θ angle. The thermal resistance of the membranes was examined by thermal gravimetric analysis Q600 (TGA, Model: Q600, USA). Next, 5–10 mg of the samples was heated from 30 °C to 800 °C with 10 °C/min rate under atmospheric pressure.

Porosity is another key parameter that determines the performance of membranes; therefore, to calculate the porosity (ε) of each membrane, first, the length, inner diameter, and outer diameter were measured. Membranes' weights were also measured after five hours of drying at 150 °C. Then, the membranes were placed in water for 12 h to fill the pores with water. The excess water on the membranes' surfaces was removed and they were weighed again to determine the weight of the wet membranes. The porosity of each membrane was calculated from the following equation [38]:

$$\varepsilon = \frac{V_s}{V_t} \times 100 \tag{10}$$

$$V_s = \frac{M_w - M_d}{\rho_w} \tag{11}$$

$$V_t = \pi {R_{out}}^2 \mathrm{L} - \pi\ {R_{in}}^2 \mathrm{L} \tag{12}$$

where:

ε: porosity
V_s: cavity volume
V_t: Total membrane volume
M_w: Wet membrane weight
M_d: Dry membrane weight
ρ_w: water density
R_{out}: external radius of the membrane
R_{in}: internal radius of the membrane

The Guerout–Elford–Ferry equation was used to measure the average pore radius (r_m) of MF membranes based on distilled water J and Porosity [39]:

$$r_m = \sqrt{\frac{(2.9 - 1.75\varepsilon)8\mu \mathrm{L} J}{\varepsilon \mathrm{TMP}}} \tag{13}$$

In fact, ε is the membrane porosity (%), L is the membrane thickness (m), μ is water viscosity at room temperature (8.9×10^{-4} Pa.s), J is water permeation per unit time ($m^3 s^{-1}$), and transmembrane pressure (TMP) is the operating pressure (0.5–2 bar).

Mechanical strength analysis (three-point flexural test) was conducted by the universal test apparatus (Santam STM-20, Iran) according to ASTM d790 standard with a strain rate of 0.5 mm/min at 25 ± 2 °C. Bending stress (σ_f) was determined from the following equation [40]:

$$\sigma_f = \frac{8Fl}{\pi d^3} \tag{14}$$

Where:

F: the force (N) at the fracture point,
l: the support span (mm)
and R: the radius of the beam (mm).

At least three samples were used to obtain the average values and the standard deviation for each membrane.

5. Results and Discussion

5.1. Membranes' Microstructures

The microstructures of the prepared membranes were studied by FESEM. Scanning electron micrographs of the kaolin, kaolin/SiC, and kaolin/SiC/iron oxide are presented

in Figure 4A–C, respectively, at different scales with different symbols. It should be noted that the micrographs of Figure 5 (row 1 and 2) are related to the surface of the membrane and the micrographs of row three are related to the cross-sectional view of membrane. The FESEM picture of kaolin (Figure 4A) shows a uniform, compact, and crack-free structure; it is also evident in the cross-section picture of the membrane (Figure 4A3). Furthermore, the morphology analysis of the kaolin membrane shows that the dominant morphology of this membrane is non-uniform pores with different and non-uniform sizes.

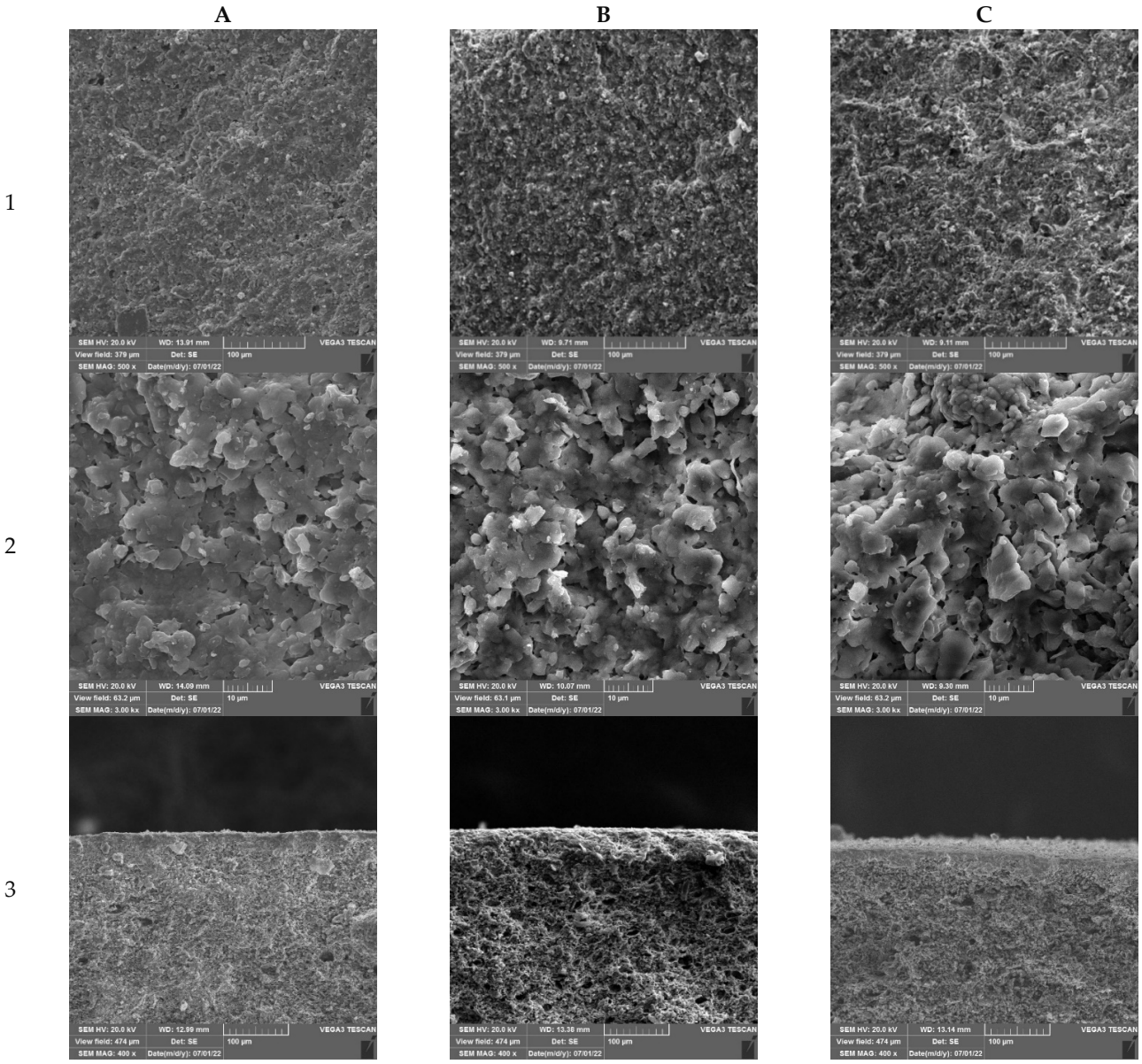

Figure 4. FESEM images of ceramic membranes M (**A**), M/SiC (**B**), and M/SiC/Fe20 (**C**).

However, the membrane structure changed after the addition of Fe_2O_3 and SiC. As shown in Figure 4B, the microstructure of SiC composite membranes is homogeneous and uniform, but it seems that the addition of SiC increased the roughness and porosity of the surface. A closer look at cross-sections of membranes reveals that the membrane surface became rougher after silicon carbide was added. Furthermore, it can be observed that the microstructure of SiC membrane has many pores with nonuniform sizes distributed all over the surface. Results of investigations indicate that the addition of Fe_2O_3 plays an

important role in membrane formation, changes in membrane morphology, and roughness of the surface [18].

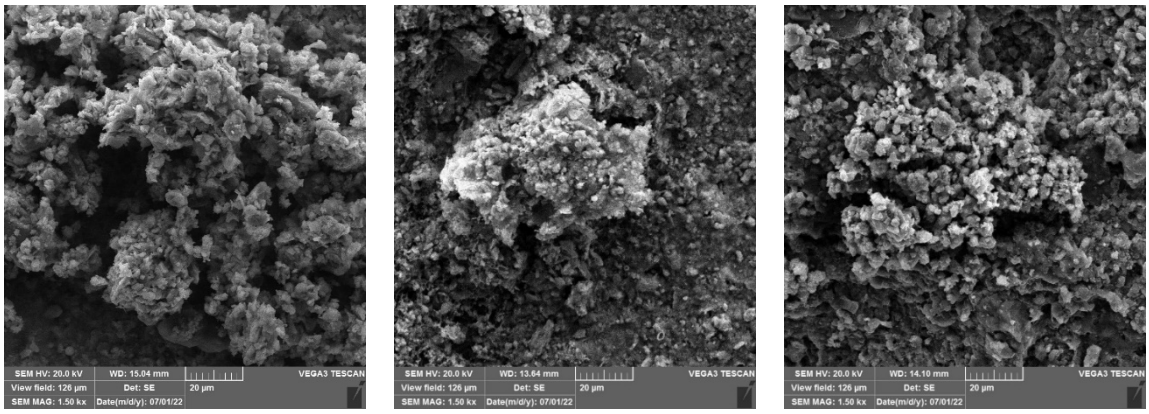

(**A**) (**B**) (**C**)

Figure 5. FESEM images of ceramic membranes M (**A**), M/SiC (**B**), and M/SiC/Fe20 (**C**) after filtration.

As seen in FESEM micrographs of M/SiC/Fe20 composite (Figure 4C), the membrane is still rough after integration with Fe_2O_3; but it seems that membrane porosity increased with a dominant sponge morphology. As indicated in Figure 4C, the number, size, and types of the pores have changed in M/SiC/Fe20 membrane compared to M/SiC30 membrane. The membrane cross-section pictures (Figure 4C3)) show a decrease in pore sizes after the addition of Fe_2O_3. Furthermore, the integration of Fe_2O_3 results in a rather rougher membrane surface. It should be noted that high roughness can significantly improve the flux [41]. Moreover, it is expected that the flux improves due to the addition of Fe_2O_3, which complies well with the theoretical and experimental data. Figure 5A–C present the scanning electron micrographs of M, M/SiC, and M/SiC/Fe20 after filtration. As seen, at the end of the filtration, a layer has formed in the pores due to the presence of dispersed particles and microorganisms in seawater, and the pores' volume is reduced.

5.2. Atomic Force Microscopy (AFM)

The surface roughness of membranes can be estimated from 2D (2-dimensional) and 3D (3-dimensional) AFM pictures. AFM analysis gives data on the morphology and roughness of the surface. The relation between these characteristics with surface porosity and filtration performance provides insight into the structure of filtration membranes. Figure 6A–C presents 2D and 3D pictures of the surface roughness of M, M/SiC, and M/SiC/Fe20 membranes. The roughness parameters, including root mean square (R_q), average roughness (R_a), and peak-to-valley roughness (R_t) were calculated and are presented in Table 4 as indicated in Figure 6. The M membrane has a relatively smooth surface with lower surface roughness (R_a = 3.72 nm) compared to other membranes. Figure 6 and data in Table 4 indicate that M/SiC/Fe20 membrane has the maximum roughness; furthermore, SEM analysis results support this subject.

Table 4. Roughness parameters obtained from atomic force microscopy.

Membrane	R_q (nm)	R_a (nm)	R_{max} (nm)
M	24.70	3.72	66.91
M/SiC	88.12	11.78	302.5
M/SiC/Fe20	203.7	26.30	394.4

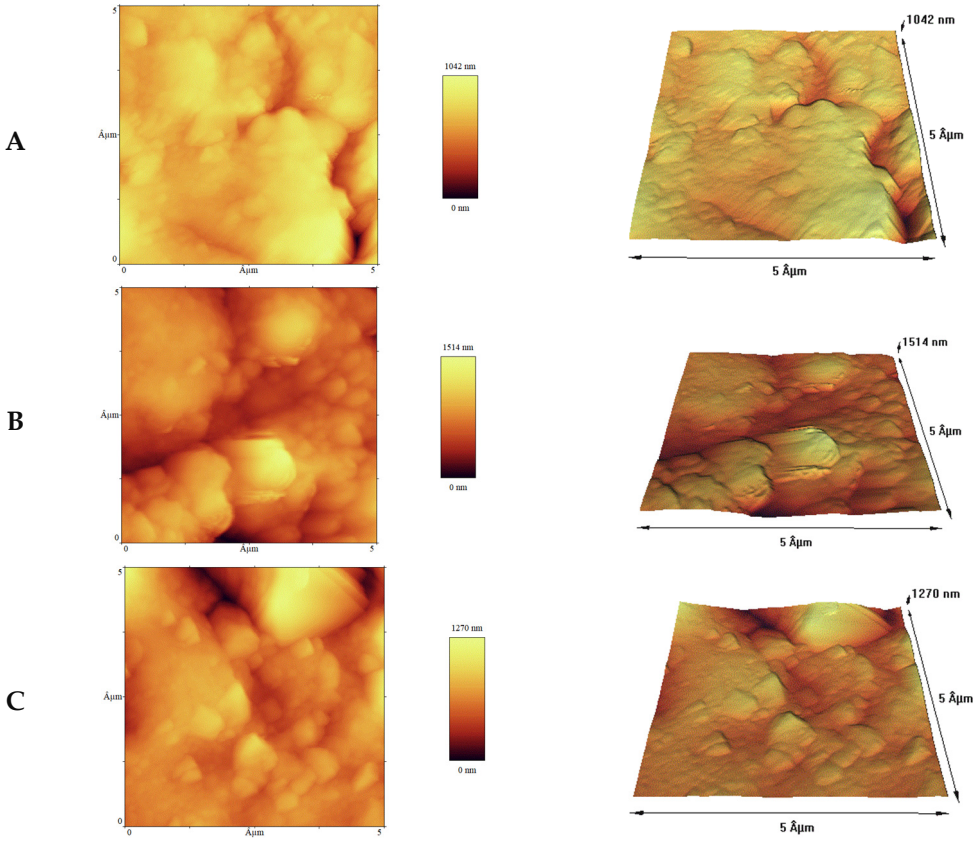

Figure 6. The roughness of membrane surface M (**A**), M/SiC (**B**), M/SiC/Fe20 (**C**).

5.3. X-ray Diffraction Analysis (XRD Analysis) of Fabricated Ceramic Membranes

XRD analysis was carried out to ensure and determine the formed phases in membranes and the structure of the as-fabricated samples after being sintering in a furnace. The XRD patterns of M, M/SiC, and M/SiC/Fe20 composites are represented in Figure 7.

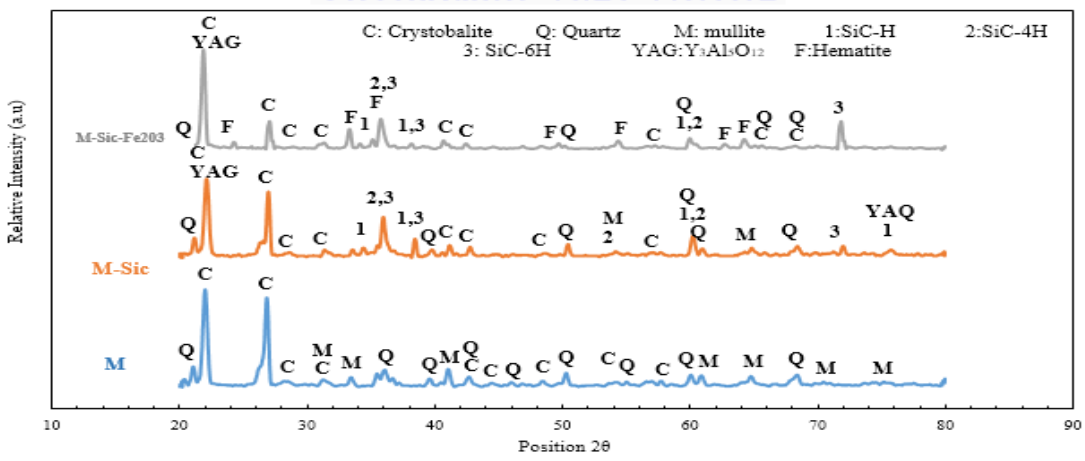

Figure 7. XRD patterns of the samples M, M/SiC and M/SiC/Fe20.

Mullite shows different ratios of Al to Si with the overall structure $Al_{4+2x}Si_{2-2x}O_{10-x}$, where x is between 0.2 and 0.8. At a temperature of 1250 °C, kaolin crystallizes into the dominant phase of quartz, cristobalite, and some mullite. The XRD pattern of the mullite sample demonstrated the characteristic peaks, which are related to cristobalite (α-Al_2O_3-SiO_2), quartz, and mullite phases. As shown in the XRD pattern of the mullite sample

(M), the characteristic peaks at around 22.06°, 26.88°, 28.90°, 32.02°, 43.32°, 44.94°, 48.94°, 56.54°, and 58.14° correspond to the cristobalite phase. Moreover, the corresponding peaks of the quartz phase can be observed at around 21.54°, 36.42°, 40.04°, 43.32°, 46.34°, 50.70°, 55.80°, 60.40°, and 68.76°. The specified peaks at 32.02°, 33.94°, 41.50°, 61.32°, 65.14°, 70.74°, and 75.40° are also characteristic peaks of the mullite phase. The presence of these peaks confirms the structure related to mullite [42–45]. In addition, the various phases of the silicon carbide composition can be clearly seen in the XRD pattern of the M-SiC sample. These phases include SiC-4H, SiC-H, SiC-6H, and yttrium aluminum ($Y_3Al_5O_{12}$). Hence, the XRD patterns of M/SiC confirm the successful synthesis of silicon carbide and its doping with mullite [45,46]. As presented in the XRD pattern of the M/SiC/Fe20 composite sample, in addition to the characteristic XRD peaks of kaolin and silicon carbide compounds, the characteristic peaks of hematite (Fe_2O_3) are also observed at about 24.80°, 33.60°, 35.40°, 49.16°, 54.80°, 63.70°, and 65.30°, which conform to crystal planes (012), (104), (110), (024), (116), (214), and (300), respectively [47]. Hence, the studies of the XRD pattern of the M/SiC/Fe20 microfiltration membrane indicate that no chemical reaction occurred between Fe_2O_3 and SiC.

5.4. Thermal Analysis of Ceramic Membranes

TGA is a powerful thermal analysis method based on weight change with temperature over time. This test provides information about thermal degradation, solid-gas reactions, phase transition, adsorption, and desorption.

Figure 8 illustrates that weight loss occurred in three different stages for microfiltration membrane M.

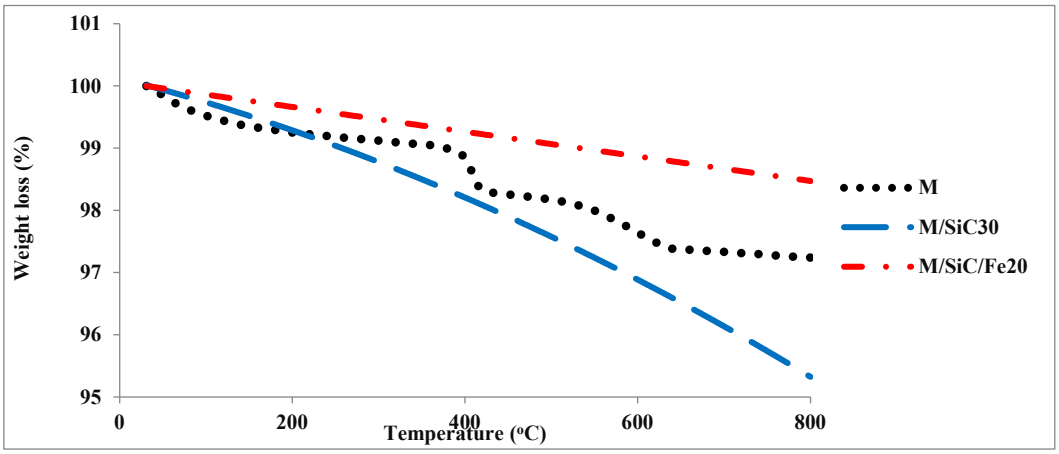

Figure 8. TGA of M, M/SiC30 and M/SiC/Fe20 microfiltration membranes.

The first stage of weight loss of the M microfiltration membrane is probably related to the removal of moisture. The second stage of weight loss occurred between 400 and 650 °C, which was the result of the phase change and the formation of metakaolin from the kaolinite phase (according to reaction (1)) [45].

$$2AL_2Si_2O_5(OH)_4 \rightarrow 2AL_2SiO_7 + 4H_2O \quad (15)$$

The third stage of weight loss can be due to the formation of mullite phase (reaction 2) [45].

$$3(AL_2O_3.2SiO_2) \rightarrow 3AL_2O_3.2SiO_2(\text{mullite}) + 4SiO_2(\text{quatz, cristobalite}) \quad (16)$$

Figure 8 also shows that the weight loss for the M/SiC microfiltration membrane is 4.7% and for the M/SiC/Fe20 membrane it is 1.6%. The results indicate that the M/SiC/Fe20 ceramic composite membrane has excellent oxidation resistance because it had the lowest amount of weight loss compared to other membranes.

5.5. Mechanical Strength Analysis of Ceramic Membranes

One of the main problems with ceramic membranes is their brittleness. Mechanical strength analysis (three-point flexural test) was performed to investigate the physical strength of the manufactured membranes. The bending strength is calculated from Equation (14). The strengths of the prepared membranes are listed in Table 5.

Table 5. Flexural stress (MPa) of MF membranes.

Membrane	Mechanical Strength (MPa)
M	19.7 ± 0.5
M/SiC10	19.5 ± 0.5
M/SiC20	19.1 ± 0.5
M/SiC30	18.7 ± 0.5
M/SiC/Fe5	21.9 ± 0.5
M/SiC/Fe10	22.4 ± 0.5
M/SiC/Fe20	19.6 ± 0.5

There is valuable information in the literature from previous studies that indicate the reduction in the bending strength of porous ceramics when the porosity increases [48,49]. Aouadia et al. indicated that, in addition to increased porosity, increasing the pore sizes of ceramic membranes can also decrease mechanical strength [50].

As seen in Table 4, the addition of silicon carbide increases the membrane porosity and the increased porosity decreases the membrane strength, these results comply well with the report of Jafari et al. [45].

In addition, the results of the investigations show that increasing the concentration of nanofillers will enhance the mechanical strength of nanocomposite membranes to a specific point, and after this optimum point, further addition of nanofillers promotes the accumulation of nanoparticles and weakens the mechanical strength. The addition of Fe_2O_3 improves the mechanical strength, since it is dissolved with other crystals and increases multization and forms a crystalline phase. Furthermore, Fe_2O_3 plays the role of a crystalline compound that improves the mechanical characteristics of the samples [51–53]. As the values in the table show, increasing Fe_2O_3 content up to 10 wt.% will increase the membranes' mechanical strength; however, further addition of Fe_2O_3 causes the formation of excess liquid and highly porous structures in the membranes and reduces the mechanical strength. These results comply well with the findings of Li et al. [54].

5.6. Porosity and the Average Pore Size

The porosity of MF membranes is calculated from Equation (3). As indicated in Table 6, the porosity of the mullite membrane is 31.3%. The addition of 30% silicon carbide to mullite increases the porosity to 43.8%; this enhanced porosity due to the addition of SiC was also reported by Jafari et al. [45].

Furthermore, we know that the structure of porous ceramics is known to depend on the size and shape of the filler grains, its ratio to the sintering strengthening fine-grained component, and on the compaction pressure, presence, and quantity of organic binders and plasticizers that facilitate the compaction, as well as on the heat treatment modes. However, adding Fe_2O_3 is closely related to the abnormal grain growth of mullite, which suppressed

the sintering behavior and alleviated the densification process and leads to an increase in porosity [55].

Table 6. Porosity and the average pore size of MF membranes.

Membrane	Porosity (%)	Average Pore Size (μm)
M	31.3 ± 2	0.48
M/SiC10	34.5 ± 3	0.55
M/SiC20	38.6 ± 2	0.57
M/SiC30	43.8 ± 3	0.59
M/SiC/Fe5	58.7 ± 2	0.56
M/SiC/Fe10	64.6 ± 2	0.54
M/SiC/Fe20	69.1 ± 1	0.52

The mean pore radius (rm) was determined according to Equation (13) and based on the pure water flux. As seen, enhanced porosity decreases the average pore size and the increased slope of permeability flux versus pressure increases the pore size. Considering the data in this table, the maximum pore radius belongs to the M/SiC30 membrane, with a value of 0.59 μm and 43.8 % porosity, and the minimum one is for the M membrane, with a value of 0.48 μm and 31.3% porosity.

5.7. Flux of Pure Water for Fabricated Membranes

Figure 9 presents the stable permeation of pure water (with <5 cm^{-1}. μs conductivity) versus membrane pressure for microfiltration membranes as a function of different pressure (0–2 bar). A strong correlation ($R^2 \geq 0.99$) between the applied pressure on all membranes and water flux indicates the absence of fouling during filtration. It is easily recognized that for all the curves, J water was increased linearly with increasing pressure. In fact, J of water is highly dependent on the porosity and average membrane pore size; therefore, the maximum J (4401 L/m^2.h at 1 bar pressure) belonged to M/SiC/Fe20 membrane, with a maximum porosity of 69.1% and average pore size of 0.52 μm, and the minimum J (1006 L/m^2.h h at 1 bar pressure) was for M membrane, with 31.3% porosity and average pore size of 0.48 μm.

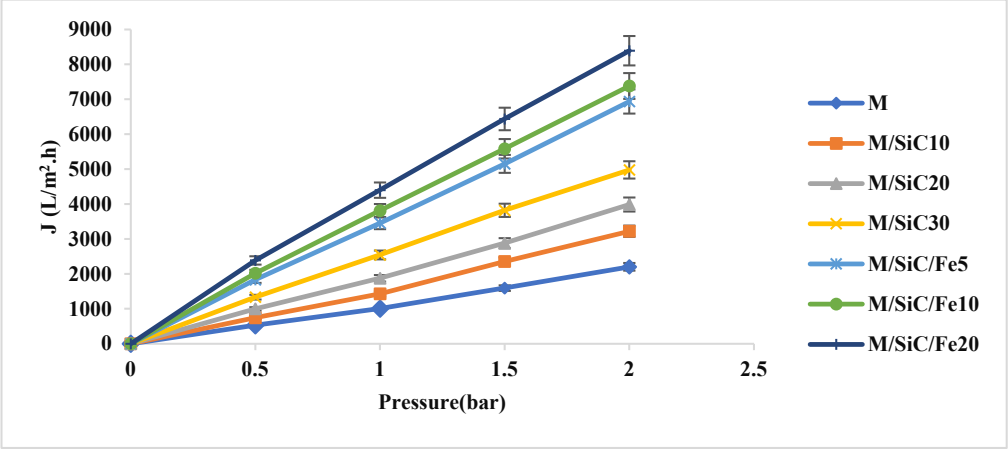

Figure 9. Effect of passing pressure on pure water flux for different microfiltration membranes.

5.8. Seawater Pre-Treatment

The results of flux versus time are presented in Figure 10 for M, M/SiC10, M/SiC20, M/SiC30, M/SiC/Fe5, M/SiC/Fe10, and M/SiC/Fe20 during seawater pre-treatment. Jafari et al. indicated that the addition of SiC to the mullite membrane increased the porosity

and hydrophilicity of the membrane surface and, thus, the flux improved compared to mullite membranes. These findings are in good accordance with our data [45]. The membrane flux boosted continuously by increasing the amount of SiC.

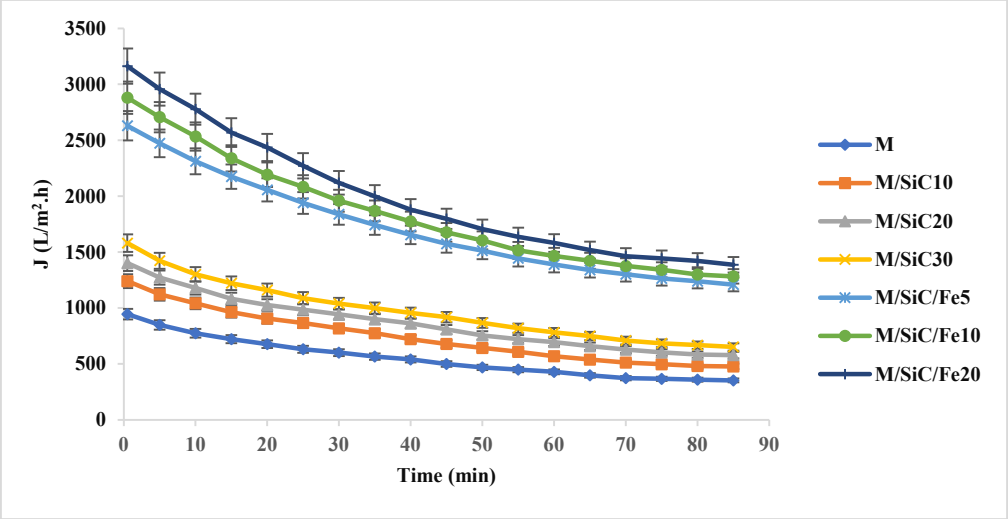

Figure 10. Variation of J of the fabricated microfiltration membranes as a function of time at 1 bar constant pressure.

Adding Fe_2O_3 to the membranes improves the hydrophilicity of the surface, which increases the interactions between the membrane surface and water, and, therefore, significantly improves the performance and flux of the membrane. The flux of Mullite/SiC/Fe_2O_3 composite membrane decreased over time, but it was still higher after 40 min of the start of the process. The integration of Fe_2O_3 particles into the composite membrane increased the porosity and resulted in enhancement of flux, which complies well with Salar-García results [55].

5.9. Turbidity Removal

The seawater quality was defined by its turbidity before passing from microfiltration membranes. The turbidity of Persian Gulf shore water was measured several times and the average obtained value was 11.64 NTU. This indicates that the Persian Gulf seawater should pass a pre-treatment stage before desalination. The amount of turbidity removal by each membrane is reported in Figure 11.

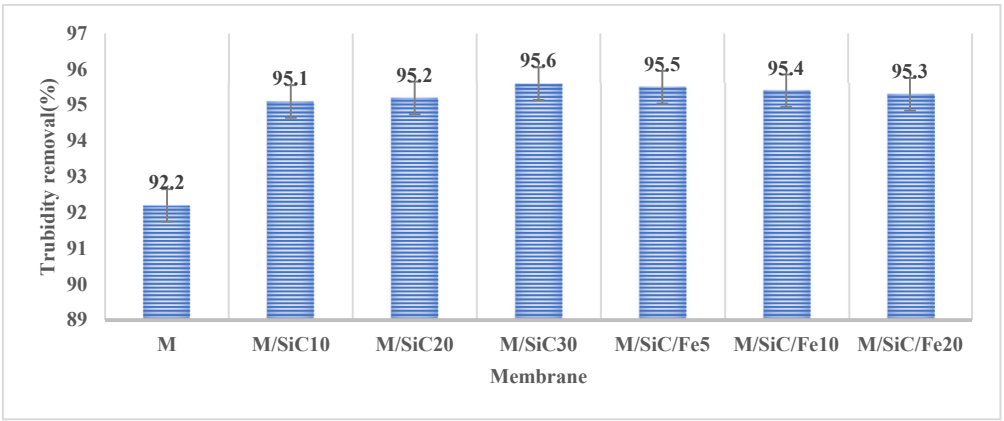

Figure 11. Turbidity removal (%) by the manufactured microfiltration membranes.

According to Figure 11, the maximum turbidity removal belongs to the M/SiC30 membrane with 95.6 % removal and the minimum one is for the M membrane with 92.2% turbidity removal.

As it is obvious, increasing silicon carbide percentage in composite membrane structure causes slight enhancement of the turbidity removal and M/SiC30 has the best performance in the removal of turbidity. Moreover, it can be seen that increasing the amount of Fe_2O_3 decreased the turbidity removal slightly, but this reduction is not considerable and can be neglected against improvement of J and mechanical strength of Fe_2O_3 membranes.

Previous studies indicated that the performance of ceramic membranes in colloidal and small particle removal is lower than in large particle removal. The main effective parameter of turbidity is the presence of large suspended particles and microorganisms [56]. Results of turbidity removal revealed that the turbidity did not change considerably by changing the membrane pore size and it is in good agreement with previous investigations.

6. Modeling

Modeling of J Reduction over Time for Microfiltration Membranes

Figure 12 presents the results of J modeling by Hermia's models (Cake formation model, mild pore blocking model, standard pore blocking model, and complete pore blocking model) for microfiltration membranes during seawater pre-treatment.

Figure 12 shows that the standard blocking model has the minimum error and the best compliance with experimental data. To determine the data compliance of each model, R^2, mean error of each model was calculated to predict *J* over the filtration time and the results are listed in Table 7.

Table 7. The mean error between experimental fluxes and the modeled ones, using Hermia's models for the manufactured microfiltration membranes.

	Cake Formation Model		**Intermediate Pore Blocking Model**		**Standard Pore Blocking Model**		**Complete Pore Blocking Model**	
	Average Error (%)	**R^2**	**Average Error (%)**	**R^2**	**Average Error (%)**	**R^2**	**Average Error (%)**	**R^2**
M	16.303	0.847	13.438	0.8857	3.907	0.994	8.124	0.947
M/SiC10	16.523	0.835	13.855	0.8759	2.523	0.996	8.983	0.941
M/SiC20	14.879	0.829	12.371	0.865	3.677	0.996	7.977	0.928
M/SiC30	14.913	0.805	12.390	0.8359	4.865	0.995	8.019	0.906
M/SiC/Fe 5	10.671	0.930	7.689	0.963	3.078	0.992	3.878	0.971
M/SiC/Fe10	13.017	0.8715	10.935	0.901	3.502	0.990	7.379	0.953
M/SiC/Fe 20	12.595	0.8955	10.385	0.9229	4.175	0.982	6.691	0.967

According to R^2 values and mean errors between the experimental and modeled permeations at all the experiments, it is observed that the regression line of the standard blocking model is in good compliance with the experimental data. As mentioned previously, the fouling mechanism occurs when the pore diameter is greater than the particle diameter, and the particles can enter membrane pores, precipitate on pore walls, and decrease the pore volume. Furthermore, this reduction in pore volume is proportional to the flux and volume.

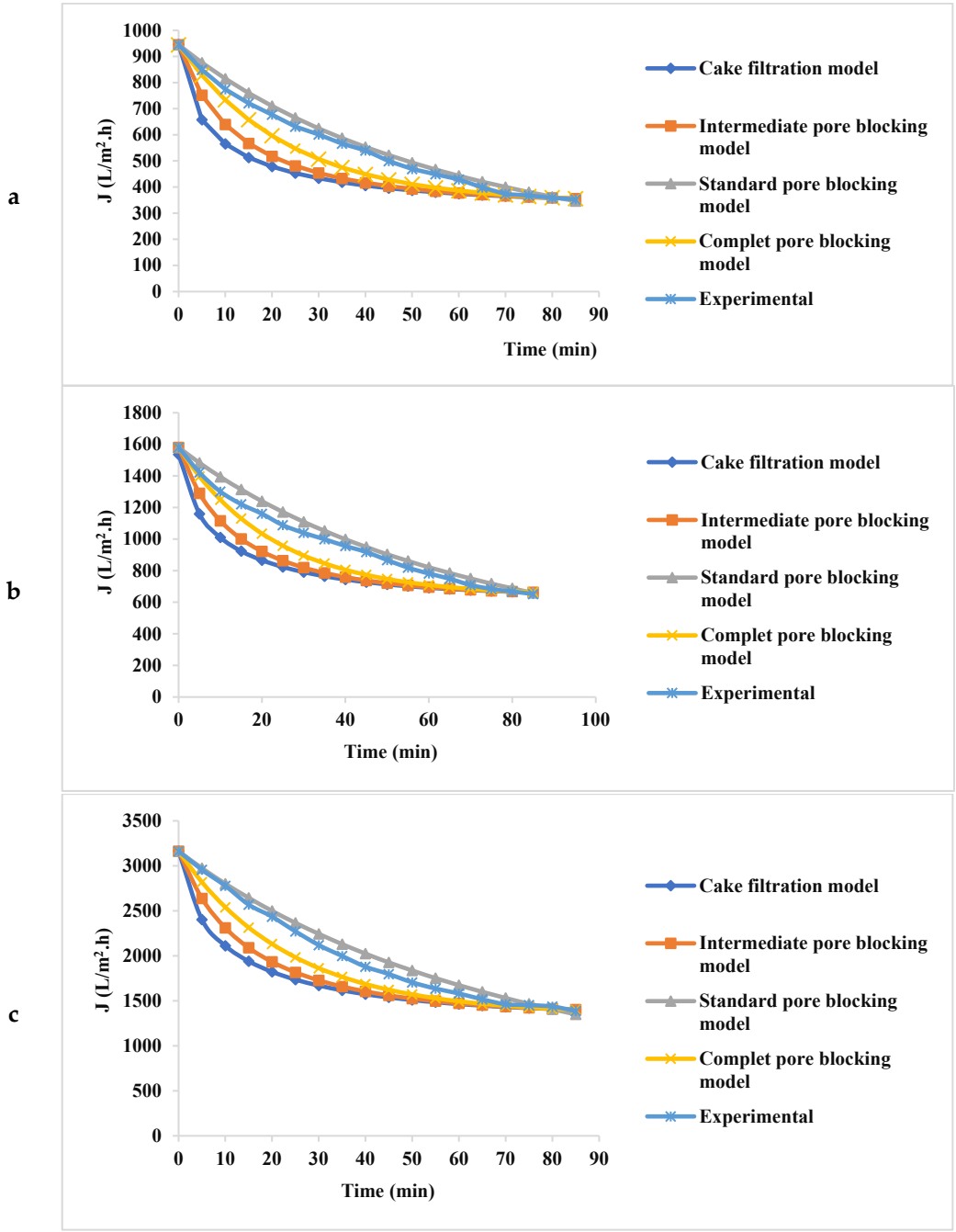

Figure 12. Variations of experimental and predicted *J* decline for (**a**) M, (**b**) M/SiC30, and (**c**) M/SiC/Fe20.

7. Conclusions

In this study, we fabricated tubular ceramic microfiltration membranes (M, M/SiC, M/SiC/Fe_2O_3) with different compositions using extrusion and sintering methods. Using kaolin as a geomaterial can decrease the production cost of silicon carbide membranes significantly by reducing the sintering temperature. Scanning electron microscopy was utilized on the surface of the prepared membranes to determine the membrane morphology, XRD was employed to ensure the crystallization and the formation of the desired phases. The porosity, average pore diameter, and membrane strength against mechanical tensions were also measured and calculated. In this study, Persian Gulf seawater was used in all

the experiments. Results indicated that utilizing SiC and iron oxide increased the surface roughness of the membranes and improved their performance by increasing the flux.

Among the manufactured membranes, the maximum pure water flux (4401 L/m^2.h) belonged to M/SiC/Fe20 membrane with 0.52 μm pore size, 69.1% porosity, and maximum surface roughness. The minimum pure water flux (1006 L/m^2.h) belonged to the M membrane with 0.48 μm pore size, 31.3% porosity, and the minimum surface roughness. Results presented that, for all the manufactured microfiltration membranes, pure water flux increased linearly with increasing the passing pressure, this enhancement can be attributed to the enhanced driving force due to the increased pressure.

Furthermore, the three-point flexural test and TGA analysis indicated that the mechanical and thermal properties of the membranes containing Fe_2O_3 have improved significantly. The fouling mechanisms in the manufactured microfiltration membranes were determined by modeling the reduction in experimental flux using Hermia's models. Results indicated that the best model for prediction of membrane fouling is the standard blocking mechanism and this mechanism has the maximum compliance with the experimental data.

Results of this investigation revealed that using M/SiC/Fe10 microfiltration membranes for seawater pre-treatment is more feasible than the other microfiltration membranes, since they have high flux (3811 L/m^2.h at 1 bar pressure), better mechanical strength (22.4 MPa), and can eliminate 95.4 % of turbidity.

Author Contributions: Conceptualization, M.Y. and M.A. (Mohsen Abbasi), methodology, M.Y. and M.A. (Mohsen Abbasi); software, M.Y. and M.A. (Mohsen Abbasi); validation, M.Y. and M.A. (Mohsen Abbasi); formal analysis, M.Y., M.A. (Mohsen Abbasi), M.S. and M.A. (Mohammad Akrami); investigation, M.Y., M.A. (Mohsen Abbasi) and M.S.; resources, M.A. (Mohsen Abbasi); data curation, M.Y. and M.A. (Mohsen Abbasi); writing—original draft preparation, M.Y.; writing—review and editing, M.Y., M.A. (Mohsen Abbasi), M.S. and M.A. (Mohammad Akrami); visualization, M.Y. and M.A. (Mohsen Abbasi); supervision, M.A. (Mohsen Abbasi); project administration, M.A. (Mohsen Abbasi) and M.A. (Mohammad Akrami) All authors have read and agreed to the published version of the manuscript.

Funding: This research received no external funding.

Institutional Review Board Statement: Not applicable.

Data Availability Statement: Not applicable.

Acknowledgments: The authors acknowledge the Mashhad Water and Wastewater Company, Iran, and Water and Wastewater of Bushehr Province Company, Iran, for their financial support.

Conflicts of Interest: The authors declare no conflict of interest.

References

1. Badruzzaman, M.; Voutchkov, N.; Weinrich, L.; Jacangelo, J.G. Selection of pretreatment technologies for seawater reverse osmosis plants: A review. *Desalination* **2019**, *449*, 78–91. [CrossRef]
2. Asrafuzzaman, M.; Fakhruddin, A.; Hossain, M. Reduction of turbidity of water using locally available natural coagulants. *Int. Sch. Res. Notices* **2011**, *632189*, 6.
3. Lim, Y.J.; Goh, K.; Kurihara, M.; Wang, R. Seawater desalination by reverse osmosis: Current development and future challenges in membrane fabrication–A review. *J. Membr. Sci* **2021**, *629*, 119292. [CrossRef]
4. Maftouh, A.; El Fatni, O.; Bouzekri, S.; Rajabi, F.; Sillanpää, M.; Butt, M.H. Economic Feasibility of Solar-Powered Reverse Osmosis Water Desalination: A Comparative Systemic Review. 2022; *priprint*. [CrossRef]
5. Kaya, C.; Sert, G.; Kabay, N.; Arda, M.; Yüksel, M.; Egemen, Ö. Pre-treatment with nanofiltration (NF) in seawater desalination—Preliminary integrated membrane tests in Urla, Turkey. *Desalination* **2015**, *369*, 10–17.
6. Kavitha, J.; Rajalakshmi, M.; Phani, A.R.; Padaki, M. Pretreatment processes for seawater reverse osmosis desalination systems—A review. *J. Water Process Eng.* **2019**, *32*, 100926. [CrossRef]
7. Wu, B.; Suwarno, S.R.; Tan, H.S.; Kim, L.H.; Hochstrasser, F.; Chong, T.H.; Burkhardt, M.; Pronk, M.; Fane, A.G. Gravity-driven microfiltration pretreatment for reverse osmosis (RO) seawater desalination: Microbial community characterization and RO performance. *Desalination* **2017**, *418*, 1–8. [CrossRef]

8. Belgada, A.; Achiou, B.; Younssi, S.A.; Charik, F.Z.; Ouammou, M.; Cody, J.A.; Benhida, R.; Khaless, K. Low-cost ceramic microfiltration membrane made from natural phosphate for pretreatment of raw seawater for desalination. *J. Eur. Ceram. Soc.* **2021**, *41*, 1613–1621. [CrossRef]
9. Gaikwad, V.; Munavalli, G. Turbidity removal by conventional and ballasted coagulation with natural coagulants. *Appl. Water Sci.* **2019**, *9*, 1–9.
10. Yang, H.-J.; Kim, H.-S. Effect of coagulation on MF/UF for removal of particles as a pretreatment in seawater desalination. *Desalination* **2009**, *247*, 45–52. [CrossRef]
11. Shon, H.K.; Vigneswaran, S.; Zareie, M.H.; Aim, R.B.; Lee, E.; Lee, J.; Cho, J.; Kim, I.S. Physico-chemical pretreatment to seawater reverse osmosis (SWRO): Organic characterization and membrane autopsy. *Desalination* **2009**, *236*, 282–290.
12. Yang, G.C.; Tsai, C.-M. Effects of starch addition on characteristics of tubular porous ceramic membrane substrates. *Desalination* **2008**, *233*, 129–136. [CrossRef]
13. Woo, Y.C.; Kim, Y.S.; Lee, J.J.; Choi, Y.; Kim, H.S. Evaluation of the different integrated pre-treatment processes for the ceramic based microfiltration. *Process Saf. Environ. Prot.* **2020**, *139*, 210–217. [CrossRef]
14. Achiou, B.; Elomari, H.; Bouazizi, A.; Karim, A.; Ouammou, M.; Albizane, A.; Bennazha, J.; Alami Younssi, S.; El Amrani, I.E. Manufacturing of tubular ceramic microfiltration membrane based on natural pozzolan for pretreatment of seawater desalination. *Desalination* **2017**, *419*, 181–187. [CrossRef]
15. Samhari, O.; Younssi, S.A.; Rabiller-Baudry, M.; Loulergue, P.; Bouhria, M.; Achiou, B.; Ouammou, M. Fabrication of flat ceramic microfiltration membrane from natural kaolinite for seawater pretreatment for desalination and wastewater clarification. *Desalin Water Treat* **2020**, *194*, 59–68. [CrossRef]
16. Mouiya, M.; Abourriche, A.; Bouazizi, A.; Benhammou, A.; El Hafiane, Y.; Abouliatim, Y.; Nibou, L.; Oumam, M.; Ouammou, M.; Smith, A.; et al. Flat ceramic microfiltration membrane based on natural clay and Moroccan phosphate for desalination and industrial wastewater treatment. *Desalination* **2018**, *427*, 42–50. [CrossRef]
17. Kang, J.S.; Sung, S.C.; Lee, J.J.; Kim, H.S. Application of ceramic membrane for seawater desalination pretreatment. *Desalination Water Treat.* **2016**, *57*, 26700–26705. [CrossRef]
18. Dey, T.; Sahoo, G.C.; Roy, S.N.; Bandyopadhyay, S. Studies on pre-treatment of seawater using tubular ceramic MF membrane of 19-channel configuration. *Int. J. Sci. Res. Publ.* **2013**, *3*, 1–5.
19. Xavier, L.A.; Fetzer, D.E.L.; de Oliveira, T.V.; Eiras, D.; Voll, F.A.P.; Vieira, R.B. Effect of stainless-steel slag concentration in the fabrication of cost-effective ceramic membranes: Seawater pre-treatment application. *Ceram. Int.* **2022**, *48*, 23273–23283. [CrossRef]
20. Farid, M.U.; Khanzada, N.K. An AK. Understanding fouling dynamics on functionalized CNT-based membranes: Mechanisms and reversibility. *Desalination* **2019**, *456*, 74–84. [CrossRef]
21. Choobar, B.G.; Shahmirzadi, M.A.A.; Kargari, A.; Manouchehri, M. Fouling mechanism identification and analysis in microfiltration of laundry wastewater. *J. Environ. Chem. Eng.* **2019**, *7*, 103030. [CrossRef]
22. Chang, I.S.; Le Clech, P.; Jefferson, B.; Judd, S. Membrane fouling in membrane bioreactors for wastewater treatment. *J. Environ. Eng.* **2002**, *128*, 1018–1029. [CrossRef]
23. Eom, J.-H.; Kim, Y.-W.; Raju, S. Processing and properties of macroporous silicon carbide ceramics: A review. *J. Asian Ceram. Soc.* **2013**, *1*, 220–242. [CrossRef]
24. Bukhari, S.Z.A.; Ha, J.H.; Lee, J.; Song, I.H. Oxidation-bonded SiC membrane for microfiltration. *J. Eur. Ceram. Soc.* **2018**, *38*, 1711–1719. [CrossRef]
25. Achiou, B.; Elomari, H.; Ouammou, M.; Albizane, A.; Bennazha, J.; Younssi, S.A.; El Amrani, I.E.; Aaddane, A. Elaboration and characterization of flat ceramic microfiltration membrane made from natural Moroccan pozzolan (Central Middle Atlas). *J. Mater Env. Sci.* **2016**, *7*, 196–204.
26. Fang, J.; Qin, G.; Wei, W.; Zhao, X.; Jiang, L. Elaboration of new ceramic membrane from spherical fly ash for microfiltration of rigid particle suspension and oil-in-water emulsion. *Desalination* **2013**, *311*, 113–126. [CrossRef]
27. Rasouli, Y.; Parivazh, M.M.; Abbasi, M.; Akrami, M. The effect of ceramic membranes' structure on the oil and ions removal in pre-treatment of the desalter unit wastewater. *Membranes* **2021**, *12*, 59. [CrossRef]
28. Belgada, A.; Charik, F.Z.; Achiou, B.; Kambuyi, T.N.; Younssi, S.A.; Beniazza, R.; Dani, A.; Benhida, R.; Ouammou, M. Optimization of phosphate/kaolinite microfiltration membrane using Box–Behnken design for treatment of industrial wastewater. *J. Environ. Chem. Eng.* **2021**, *9*, 104972. [CrossRef]
29. Hou, Z.; Cui, B.; Liu, L.; Liu, Q. Effect of the different additives on the fabrication of porous kaolin-based mullite ceramics. *Ceram. Int.* **2016**, *42*, 17254–17258. [CrossRef]
30. Oliveira, S.S.L.; Apolônio, T.G.; Ferreira, R.S.B.; Medeiros, V.N.; Araújo, E.M.; Lira, H.L. Silicon carbide hollow fiber membranes developed for the textile industry wastewater treatment. *Cerâmica* **2021**, *67*, 188–195. [CrossRef]
31. Lee, W.; Jayaseelan, D.; Zhang, S. Solid–liquid interactions: The key to microstructural evolution in ceramics. *J. Eur. Ceram. Soc.* **2008**, *28*, 1517–1525. [CrossRef]
32. Eom, J.-H.; Kim, Y.-W. Effect of additive composition on microstructure and strength of porous silicon carbide ceramics. *J. Mater. Sci.* **2009**, *44*, 4482–4486. [CrossRef]
33. Hubadillah, S.K.; Othman, M.H.D.; Matsuura, T.; Ismail, A.F.; Rahman, M.A.; Harun, Z.; Jaafar, J.; Nomura, M. Fabrications and applications of low cost ceramic membrane from kaolin: A comprehensive review. *Ceram. Int.* **2018**, *44*, 4538–4560. [CrossRef]

34. Arzani, M.; Mahdavi, H.R.; Sheikhi, M.; Mohammadi, T.; Bakhtiari, O. Ceramic monolith as microfiltration membrane: Preparation, characterization and performance evaluation. *Appl. Clay Sci.* **2018**, *161*, 456–463. [CrossRef]
35. Hermia, J. Constant pressure blocking filtration laws: Application to power-law non-Newtonian fluids. *Trans. Inst. Chem. Eng.* **1982**, *60*, 183–187.
36. Abbasi, M.; Taheri, A. Selecting model for treatment of oily wastewater by MF-PAC hybrid process using mullite-alumina ceramic membranes. *J. Water Chem. Technol.* **2016**, *38*, 173–180. [CrossRef]
37. Field, R.W.; Wu, D.; Howell, J.A.; Gupta, B.B. Critical flux concept for microfiltration fouling. *J. Membr. Sci.* **1995**, *100*, 259–272. [CrossRef]
38. Rasouli, Y.; Abbasi, M.; Hashemifard, S.A. Investigation of in-line coagulation-MF hybrid process for oily wastewater treatment by using novel ceramic membranes. *J. Clean. Prod.* **2017**, *161*, 545–559. [CrossRef]
39. Jafari, B.; Abbasi, M.; Hashemifard, S.A.; Sillanpää, M. Elaboration and characterization of novel two-layer tubular ceramic membranes by coating natural zeolite and activated carbon on mullite-alumina-zeolite support: Application for oily wastewater treatment. *J. Asian Ceram. Soc.* **2020**, *8*, 848–861. [CrossRef]
40. Temenoff, J.S.; Mikos, A.G. *Biomaterials: The Intersection of Biology and Materials Science*; Pearson/Prentice Hall Upper Saddle River: Upper Saddle River, NJ, USA, 2008; Volume 1.
41. Lee, D.; Cha, Y.J.; Baek, Y.; Choi, S.S.; Lee, Y. Relationships among Permeability, Membrane Roughness, and Eukaryote Inhabitation during Submerged Gravity-Driven Membrane (GDM) Filtration. *Appl. Sci.* **2020**, *10*, 8111. [CrossRef]
42. Schneider, H.; Schreuer, J.; Hildmann, B. Structure and properties of mullite—A review. *J. Eur. Ceram. Soc.* **2008**, *28*, 329–344. [CrossRef]
43. Dana, K.; Das, S.; Das, S.K. Effect of substitution of fly ash for quartz in triaxial kaolin–quartz–feldspar system. *J. Eur. Ceram. Soc.* **2004**, *24*, 3169–3175. [CrossRef]
44. Ayala-Landeros, J.G.; Saucedo-Rivalcoba, V.; Bribiesca-Vasquez, S.; Castaño, V.M.; Martínez-Hernández, A.L.; Velasco-Santos, C. Influence of corn flour as pore forming agent on porous ceramic material based mullite: Morphology and mechanical properties. *Sci. Sinter.* **2016**, *48*, 29–39. [CrossRef]
45. Jafari, B.; Rezaei, E.; Dianat, M.J.; Abbasi, M.; Hashemifard, S.A.; Khosravi, A.; Sillanpää, M. Development of a new composite ceramic membrane from mullite, silicon carbide and activated carbon for treating greywater. *Ceram. Int.* **2021**, *47*, 34667–34675. [CrossRef]
46. Ortiz, A.L.; Sanchez-Bajo, F.; Cumbrera, F.L.; Guiberteau, F. X-ray powder diffraction analysis of a silicon carbide-based ceramic. *Mater. Lett.* **2001**, *49*, 137–145. [CrossRef]
47. Qayoom, M.; Shah, K.A.; Pandit, A.H.; Firdous, A.; Dar, G.N. Dielectric and electrical studies on iron oxide (α-Fe2O3) nanoparticles synthesized by modified solution combustion reaction for microwave applications. *J. Electroceram.* **2020**, *45*, 7–14. [CrossRef]
48. Kumar, B.M.; Kim, Y.-W. Processing of polysiloxane-derived porous ceramics: A review. *Sci. Technol. Adv. Mater.* **2010**, *11*, 044303. [CrossRef]
49. Kim, S.C.; Kim, Y.-W.; Song, I.-H. Processing and properties of glass-bonded silicon carbide membrane supports. *J. Eur. Ceram. Soc.* **2017**, *37*, 1225–1232. [CrossRef]
50. Aouadja, F.; Bouzerara, F.; Guvenc, C.M.; Demir, M.M. Fabrication and properties of novel porous ceramic membrane supports from the (Sig) diatomite and alumina mixtures. *Boletín De La Soc. Española De Cerámica Y Vidr.* **2021**, *280*, 1–10. [CrossRef]
51. Iya, S.G.D.; Noh, M.Z.; Razak, S.N.A.; Sharip, N.; Kutty, A.A. Effect of Iron (111) Oxide (Fe_2O_3) as an Additive and substitution of quartz with POFA on physico-mechanical properties of porcelain. *Int. J. Nanoelectron. Mater.* **2019**, *12*, 175–184.
52. Shahsavari, P.; Eftekhari Yekta, B.; Marghussian, V. High Strength Pyroxene-Based Glass-Ceramic Foams in the Presence of Fe_2O_3. *Iran. J. Mater. Sci. Eng.* **2020**, *17*, 1–10.
53. Goh, P.S.; Ng, B.C.; Lau, W.J.; Ismail, A.F. Inorganic nanomaterials in polymeric ultrafiltration membranes for water treatment. *Sep. Purif. Rev.* **2015**, *44*, 216–249. [CrossRef]
54. Li, Y.; Zhao, L.H.; Wang, Y.K.; Cang, D.Q. Effects of Fe_2O_3 on the properties of ceramics from steel slag. *Int. J. Miner. Metall. Mater.* **2018**, *25*, 413–419. [CrossRef]
55. Salar-García, M.J.; Walter, X.A.; Gurauskis, J.; de Ramón Fernández, A.; Ieropoulos, I. Effect of iron oxide content and microstructural porosity on the performance of ceramic membranes as microbial fuel cell separators. *Electrochim. Acta* **2021**, *367*, 137385. [CrossRef]
56. Cui, Z.; Peng, W.; Fan, Y.; Xing, W.; Xu, N. Ceramic membrane filtration as seawater RO pre-treatment: Influencing factors on the ceramic membrane flux and quality. *Desalination Water Treat.* **2013**, *51*, 2575–2583. [CrossRef]